

PAPER

Mitigating leakage errors due to cavity modes in a superconducting quantum computer

To cite this article: T G McConkey *et al* 2018 *Quantum Sci. Technol.* **3** 034004

View the [article online](#) for updates and enhancements.

You may also like

- [Two-qubit gate operations in superconducting circuits with strong coupling and weak anharmonicity](#)
Xin-You Lü, S Ashhab, Wei Cui et al.
- [Escaping Detrimental Interactions with Microwave-Dressed Transmon Qubits](#)
Z. T. Wang, , Peng Zhao et al.
- [NMR imaging analogue of the individual qubit operations in superconducting flux-qubit chains](#)
Toshiyuki Fujii, Shigemasa Matsuo and Noriyuki Hatakenaka



Easy-to-use and Helium-3 free
cryogenics solutions

LEARN MORE

Quantum Science and Technology



PAPER


Mitigating leakage errors due to cavity modes in a superconducting quantum computer

RECEIVED
7 October 2017

REVISED
4 April 2018

ACCEPTED FOR PUBLICATION
11 April 2018

PUBLISHED
3 May 2018

T G McConkey^{1,2}, J H Béjanin^{1,3}, C T Earnest^{1,3}, C R H McRae^{1,3,4}, Z Pagel^{1,3,5}, J R Rinehart^{1,3} and M Mariantoni^{1,3} 

¹ Institute for Quantum Computing, University of Waterloo, 200 University Avenue West, Waterloo, Ontario N2L 3G1, Canada

² Department of Electrical and Computer Engineering, University of Waterloo, 200 University Avenue West, Waterloo, Ontario N2L 3G1, Canada

³ Department of Physics and Astronomy, University of Waterloo, 200 University Avenue West, Waterloo, Ontario N2L 3G1, Canada

⁴ Present address: National Institute of Standards and Technology (NIST), 325 Broadway, Boulder, Colorado 80305-3337, United States of America.

⁵ Present address: Department of Physics, University of California, Berkeley, 366 LeConte Hall, MC 7300 Berkeley, California 94720-7300, United States of America.

E-mail: matteo.mariantoni@uwaterloo.ca

Keywords: quantum computing, scalable architectures, quantum socket, coherent errors, box modes, superconducting qubits, substrate modes

Abstract

A practical quantum computer requires quantum bit (qubit) operations with low error probabilities in extensible architectures. We study a packaging method that makes it possible to address hundreds of superconducting qubits by means of coaxial Pogo pins. A qubit chip is housed in a superconducting box, where both box and chip dimensions lead to unwanted modes that can interfere with qubit operations. We analyze these interference effects in the context of qubit coherent leakage and qubit decoherence induced by damped modes. We propose two methods, *half-wave fencing* and *antinode pinning*, to mitigate the resulting errors by detuning the resonance frequency of the modes from the qubit frequency. We perform electromagnetic field simulations indicating that the resonance frequency of the modes increases with the number of installed pins and can be engineered to be significantly higher than the highest qubit frequency. We estimate that the error probabilities and decoherence rates due to suitably shifted modes in realistic scenarios can be up to two orders of magnitude lower than the state-of-the-art superconducting qubit error and decoherence rates. Our methods can be extended to different types of packages that do not rely on Pogo pins. Conductive bump bonds, for example, can serve the same purpose in qubit architectures based on flip chip technology. Metalized vias, instead, can be used to mitigate modes due to the increasing size of the dielectric substrate on which qubit arrays are patterned.

1. Introduction

The implementation of a practical quantum computer will make it possible to run certain algorithms much more efficiently than any classical computer [1]. Search and optimization as well as cryptography algorithms, such as Shor's algorithm, will have profound implications on society at large. Quantum walk and quantum linear equation algorithms as well as digital quantum simulation algorithms will have an important impact on scientific research. Other approaches to quantum computation, e.g., the quantum adiabatic algorithm, may also lead to relevant short-term applications such as the solution of constraint satisfaction problems [2].

Many implementations of the quantum computer and its primary component, the quantum bit or qubit, are currently under consideration [3]. Among these, superconducting qubits [4, 5] occupy a leading position due to the potential for scalability [6, 7] and robustness to dissipative phenomena [8–10]. In fact, superconducting qubits can be fabricated on a chip using standard lithography techniques and can be operated with available microwave electronics. It has been shown that the error probabilities associated with the operation of these

qubits can be as low as $\bar{p} \sim 10^{-3}$ [11, 12]. While such error probabilities are remarkable for a quantum-mechanical system, they are at least ten orders of magnitude higher than those necessary to run advanced quantum algorithms [13].

It is believed that reaching the required error probabilities can be accomplished by means of quantum error correction (QEC) algorithms [14], where quantum information is encoded in a large array of qubits. For example, a proof-of-concept implementation of the most forgiving QEC algorithm, the surface code [13], can be realized with an ensemble of about 100 qubits. A similarly sized system may also make it possible to achieve quantum supremacy, i.e., to outperform the most advanced classical supercomputer on specific problems, without resorting to QEC [15].

The operation of an array with 100 or more superconducting qubits, i.e., a medium-scale quantum processor, requires a complex classical infrastructure for qubit wiring, packaging, control, and measurement [7, 16–20]. This infrastructure almost certainly leads to new sources of qubit error, such as correlated [21] and leakage errors [22–24].

In this article, we study the detrimental effects on qubit operations due to the size of the quantum processor's package. We focus on the interaction between a qubit and an unwanted cavity mode, where this can be a *box* or *substrate mode*. The substrate is a dielectric parallelepiped on the surface of which the qubit array is fabricated; the box is the package's internal cavity above the surface of the substrate. We show that an unwanted cavity-qubit interaction [16, 25, 26] can lead to coherent leakage error probabilities well above \bar{p} .

We propose two methods to mitigate coherent leakage errors, both based on the detuning of the cavity-qubit frequency. This is realized by introducing an array of boundary conditions inside the cavity, causing the cavity frequency to shift with respect to the qubit frequency. By means of numerical simulations we demonstrate that for a cavity-qubit frequency detuning larger than $\sim 20\%$ of the qubit frequency, the coherent leakage error probability is far below \bar{p} .

The article is organized as follows. In section 2, we provide the motivation for this work. In section 3, we introduce the methods required to obtain the results exposed in section 4. In section 5, we discuss a generalization of our methods and, finally, in section 6 we outline the next steps for the experimental verification of our results. The article is completed by three appendices: qubit coherent errors and the Jaynes–Cummings model (appendix A); estimate of box-qubit coupling rates (appendix B); nonideal-case simulations and scalable implementation (appendix C).

2. Motivation

A quantum computer can be described by a purely unitary generator \mathcal{H} and a purely dissipative generator \mathcal{D} [24, 27] (see appendix A.1). The generator \mathcal{H} describes both wanted and unwanted dynamics, where the latter are called *coherent errors*. When such errors bring quantum information outside the computational subspace, they are called *coherent leakage errors*. The generator \mathcal{D} , instead, describes *incoherent leakage errors*.

Considering the interaction between one unwanted cavity mode and one qubit, the unitary generator can be written as $\mathcal{H}_{JC} = -i[\hat{H}_{JC}, \hat{\rho}]$, where \hat{H}_{JC} is the Jaynes–Cummings Hamiltonian [28], $\hat{\rho}$ is the cavity-qubit density matrix, and $i^2 = -1$; the generator \mathcal{D} accounts for cavity and qubit decoherence. The time evolution of $(\mathcal{H}_{JC} + \mathcal{D})$ can lead to leakage errors. In this case, the interplay between the coherent and incoherent error regimes is dictated by: the cavity-qubit coupling rate g ; the detuning between the qubit with transition frequency f_q and the cavity mode with resonance frequency f_c , $\Delta = (f_c - f_q)$; the cavity damping rate κ and the qubit relaxation and dephasing rates γ_r and γ_d , respectively.

In this work, we show that unwanted cavity-qubit coupling rates can be comparable to those typically used for qubit gate and readout operations [11, 12] and much larger than the state-of-the-art qubit decoherence rates [8–10]. We study the interaction between one unwanted mode and a qubit in the one excitation sector and in absence of any damping. This allows us to characterize pure coherent leakage errors by defining an upper bound for the error probability p . Additionally, we consider the case of a damped mode by analyzing the incoherent errors due to the Purcell rate Γ_c . In both cases, we demonstrate that by suitably increasing Δ and decreasing κ results in $p \ll \bar{p}$ and $\Gamma_c \ll \gamma_r$ (see section 4). The case of multiple modes is discussed in section 5. Although it would be possible to achieve similar results by decreasing g , this is not a scalable solution for typical package and qubit designs (see section 5).

The resonance frequencies of a cavity are determined by the electromagnetic field boundary conditions, which can be modified to shift these frequencies. In the case of a cavity-qubit system this results in a change of Δ . Although there are many possible approaches to achieve this goal, we investigate two *frequency shifting methods* based on appropriately designed arrays of zero-potential boundary conditions: *Half-wave fencing* and *antinode pinning*. Half-wave fencing, inspired by the picket fence Faraday cage, provides a straightforward analytical solution that can be used to quickly estimate the resources required for the desired change in Δ . In the case of

perfect conductors, antinode pinning provides the optimal method to modify boundary conditions, transforming cavity mode antinodes into nodes through an iterative procedure. As suggested by our findings, a combination of these methods allow an optimized usage of resources for the mitigation of qubit coherent leakage errors.

The practical implementation of our methods requires the qubit array design to account for the package design, and vice versa. Limitations dictated by the end user's specifications, such as fixed circuit placement, must be carefully taken into consideration. In an ideal process, the array of boundary conditions required for a desired shift in Δ is first determined, followed by the design of the qubit array and placement of the qubit control and measurement wires. For the greatest optimization, the design of the entire system should be performed iteratively with the assistance of full electromagnetic field numerical simulations.

In order to test the efficacy of our methods, we consider the medium-scale quantum processor introduced in [29], where it is shown that a 10×10 array of Xmon transmon qubits [8] can be realized on a $72 \text{ mm} \times 72 \text{ mm}$ dielectric substrate in a box with similar lateral dimensions. This box leads to unwanted modes with resonance frequency in the region of the qubits transition frequency. Very similar architectures have been envisioned and implemented by other research groups [17, 20]. A common feature to these architectures is the metalization of almost the entire substrate surface, the majority of which serves as a ground plane. The area of dielectric exposed to the box due to the required circuit components is low enough not to significantly perturb the modes of the system, nor do the circuits themselves (see appendix C). This feature allows us to study and propose remedies for box and substrate modes independently, as well as to ignore specific circuit designs.

We note that the packaging method proposed for the quantum processor in [29] has been defined the *quantum socket* or, by other users, plane breaking package [20]. This, which is the packaging method used in our laboratory, differs significantly from other packaging solutions as it is based on coaxial Pogo pins instead of wire bonds [25] or bump bonds [17, 18, 30, 31]. The Pogo pins used in our package are custom-made, spring-loaded coaxial microwires with an outer diameter of $1290 \mu\text{m}$; the mechanical and electrical properties of the pins have been studied in detail in [29].

The pins can serve the twofold functionality of addressing the qubit array for quantum operations and acting as a zero-potential boundary condition for the box (see section 4.1). For the medium-scale quantum processor analyzed here, the number of pins required to address the qubits is enough to sufficiently reduce leakage errors due to box modes when applying one of our frequency shifting methods. Furthermore, we show that for boxes with lateral dimensions up to $1 \text{ m} \times 1 \text{ m}$ the number of pins required by the methods is on the same order of or less (in some instances significantly less) than those necessary to control and measure the qubits, e.g., in a surface code architecture as in [29]. This will not always be the case for all quantum processors, where zero-potential boundary conditions in addition to those naturally provided by the wiring array may be required (see section 5). It is worth noting that conducting elements other than coaxial Pogo pins can alternatively be used as boundary conditions, such as bump bonds to remove box modes or metalized vias [17, 32] to remove substrate modes (see section 5).

3. Methods

In this section, we introduce the half-wave fencing and antinode pinning methods (see sections 3.1 and 3.2, respectively). We then describe the setup and settings of the electromagnetic field simulations performed to study the effects of coaxial Pogo pins on box modes (see section 3.3). Finally, we present a theoretical model to calculate the coherent leakage error probability and dispersive Purcell rate for a qubit coupled to an unwanted cavity mode (see section 3.4).

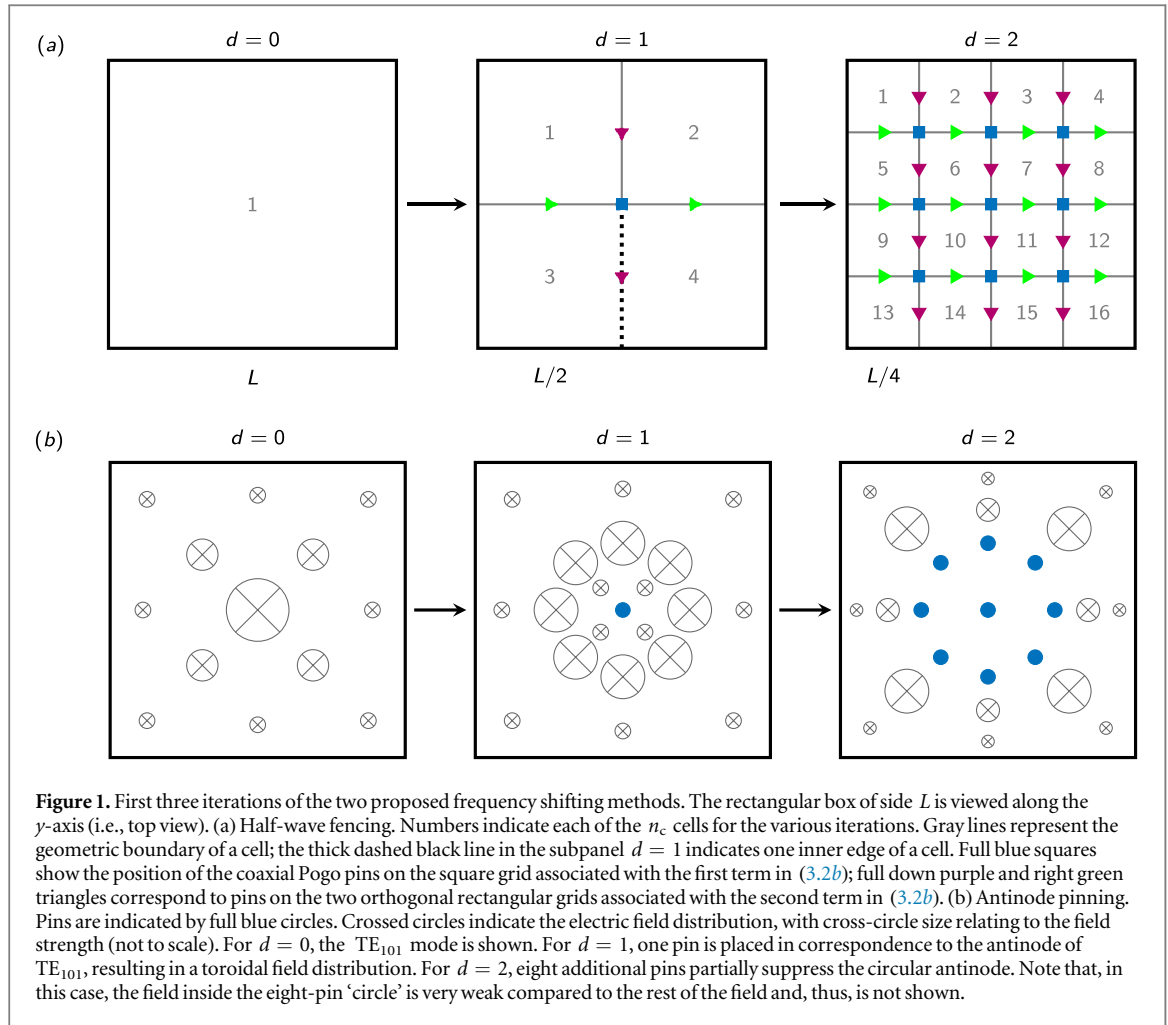
3.1. Half-wave fencing

The inner space of a microwave package can be modeled by a box with square cross-section of side length L and height H . The box supports both transverse electric (TE) and transverse magnetic (TM) modes with resonance frequencies [33]

$$f_{nm\ell} = \frac{c}{2} \left(\frac{\ell^2 + n^2}{L^2} + \frac{m^2}{H^2} \right)^{1/2}, \quad (3.1)$$

where c is the velocity of light in vacuum and $n, m, \ell \in \mathbb{N}$ refer to the number of half wavelengths spanned by the electromagnetic field in the x -, y -, and z -axis.

When $L > H$, the mode with the lowest resonance frequency or dominant mode is the $\text{TE}_{nm\ell} = \text{TE}_{101}$ mode. The corresponding resonance frequency is $f_{101} = c/(\sqrt{2}L)$. Under these conditions, the box can be represented by a two-dimensional square membrane with side L , as shown in figure 1(a). The L^2 square can be iteratively divided into smaller squares with dimensions $\{(L/2^1)^2, (L/2^2)^2, \dots, [L/(2^d)]^2\}$, where $d \in \mathbb{N}_{>0}$ is



the number of iterations (except for the 0th iteration). The total number of squares after d iterations is thus $n_c = 2^{2d}$.

The physical implementation of this method is realized by dividing the box in a number n_c of smaller boxes or *cells*, which are encapsulated by perfectly conducting grounded walls; each cell behaves as a Faraday cage. The walls can be replaced by a large set of coaxial Pogo pins, resulting in a Faraday picket fence. Figure 1(a) displays the fences for $d = 0, 1, 2$. The iteration $d = 1$, for example, comprises one vertical and one horizontal fence. In the simplest case, each of these two fences can be approximated by three equally separated pins, one of which is in the center of the L^2 cell (with the center pin being used only once). This method, which we name half-wave fencing, makes it possible to shield pairs of adjacent cells. After d iterations, the frequency of the lowest resonant mode for each of the n_c cells and the total number of pins are given by

$$f_c = f_{101} 2^d, \quad (3.2a)$$

$$N = (2^d - 1)^2 + 2 \times 2^d (2^d - 1), \quad (3.2b)$$

respectively, where $N \in \mathbb{N}$ is obtained from a simple counting argument (see figure 1(a) for a schematic pin counting representation). As expected, f_c increases with d (the smaller the cell, the higher the resonance frequency). By substituting the expression for 2^d obtained from (3.2a) into (3.2b), we obtain a quadratic equation in the variable f_c/f_{101} with parameter N . By selecting the positive solution of this equation, we find an analytic expression for f_c as a function of N , which reads

$$f_c = \frac{f_{101}}{3} (2 + \sqrt{1 + 3N}). \quad (3.3)$$

In practice, this equation is only valid for values of N corresponding to integer values of d given by (3.2b), which are associated with an even number of half-wave fenced cells of equal size. However, interpolating (3.3) for arbitrary integer values of N and, more in general, for real values of N (this would correspond to fractional portions of a pin and, thus, have no actual physical meaning) helps understand qualitatively the frequency shifting trend offered by the method (see examples in section 4.2).

The working principle of half-wave fencing is to introduce enough pins to shift the lowest resonance frequency of a cell to a certain value f_c , maintaining the distance λ between any pair of pins in a fence to be half of the wavelength associated with f_c , $\lambda = c/(4f_c)$. This approach allows us to optimize resources while achieving a reasonable shielding against electromagnetic fields with frequency f_c . For modes with resonance frequency much higher than f_c , the vacuum gaps between the pickets make the cells practically transparent to the field. This, however, is not a major concern if those modes are already well separated in frequency from the qubit transition frequency f_q , $f_c \gg f_q$. In fact, if this is not the case more steps of the method have to be applied to sufficiently shift the frequency of lower modes.

In order to better understand the applicability of the method in realistic implementations, it is worth providing an example. Suppose the user has $N = 33$ pins at their disposal, corresponding exactly to $d = 2$. Following our protocol the entire box can be split into $n_c = 16$ fully half-wave fenced cells. However, the user may opt to form only four cells, using eight pins on each inner edge with one pin in the center. While this approach would realize a higher density picket fence on each edge (thus mimicking more closely the case of four fully walled cells), the numerical simulations reported in section 4.1 show that resorting to the half-wave fencing method remains the better approach.

Once a fully half-wave fenced cell for a certain value of d is formed, the cell volume is $V = a^2 H$, where $a = L/2^d$ and H is maintained constant. The corresponding zero-point electric field for the lowest resonant mode of the cell is obtained from (A.1) and reads

$$E_{c0} = \frac{1}{c} \left(\frac{h f_c^3}{\varepsilon_0 H} \right)^{1/2}, \quad (3.4)$$

where ε_0 is the electric constant and h the Planck constant. Note that this equation is valid up to a certain frequency cutoff dictated by the smallest cell size⁶.

3.2. Antinode pinning

An alternative method to increase the resonance frequency of the modes in a rectangular box can be realized by introducing new zero-potential boundary conditions at the antinodes of the box electric field \vec{E} , i.e., where $\|\vec{E}\|$ is maximum. Each new boundary condition suppresses the corresponding antinode, thus effectively transforming it into a node. Even though such boundary conditions can be physically implemented in various ways, we focus on coaxial Pogo pins the conductive nature of which forces $\|\vec{E}\| = 0$. Figure 1(b) displays the first three iterations of the algorithm used to perform this method, which we name antinode pinning.

The spatial distribution of the electric field associated with the TE_{101} mode is characterized by a sinusoidal shape; the field antinode is located at the center of the box. When introducing a pin at this location, iteration $d = 1$, the dominant mode (and all other modes) increases in frequency and the field distribution no longer resembles that of a $TE_{nm\ell}$ mode. In this case, $\|\vec{E}\|$ has a toroidal structure with a continuous antinode distribution of circular shape.

The pins, however, can only be placed at semi-discrete locations. Thus, when performing iteration $d = 2$, it is only possible to partially suppress the entire antinode distribution by means of a finite number of pins. The performance of the method improves with the number of pins, until reaching the limit where the pins start touching each other.

In subsequent iterations, the specific pin placement for continuous antinode distributions significantly impacts the overall performance of the antinode pinning method, as discussed in section 4.1. In addition, the box modes depart from a simple geometric structure that can be described with analytical functions. Under these conditions, the pin placement and corresponding electromagnetic field distribution must be determined through numerical simulations. These can be simplified by solving the two-dimensional wave equation, i.e., ignoring the y -axis, assuming the pins to be additional boundary conditions. It is possible to perform the antinode pinning method efficiently by executing the algorithm of figure 1(b) automatically until a desired frequency or maximum number of pins is reached.

3.3. Electromagnetic field simulations setup and settings

In order to study in detail the effects of the frequency shifting methods on unwanted box modes, we resort to numerical simulations of the electromagnetic field using the high-frequency three-dimensional full-wave electromagnetic field simulation software (also known as HFSS) by Ansys, Inc.⁷

The typical model used in our simulations is an ideal box with dimensions $L = 72$ mm and $H = 3$ mm, which is simulated by means of the HFSS eigenmode solution type. When considering a large number of coaxial

⁶ That is, $f_c \rightarrow +\infty$.

⁷ See <http://ansys.com/products/electronics/ansys-hfss> for details on HFSS.

Pogo pins inside the box, the electric field distribution is initially unknown. Thus, we do not make use of any mesh operation at the beginning of the simulation, instead allowing the adaptive meshing procedure to determine the optimal meshing layout. A maximum delta frequency pass of 0.01% is used, with a minimum converged pass count of 3. For large values of d the simulations fail to converge as the mesh density required exceeds the memory capacity of our computer.

In the case of the antinode pinning method, we solve for the dominant eigenmode of a certain model that is then overlaid with the resulting $\|\vec{E}\|$. To suppress the antinode of this eigenmode, we assume perfectly conducting coaxial pins with given diameter (see section 4.1). We note that the actual outer conductor of the pins used in our packages is made from brass [29]. However, the thickness of this conductor is orders of magnitude larger than the skin depth and, thus, the perfect conductor idealization can be safely used. After pinning the antinode, we solve again for the dominant eigenmode and repeat the procedure by placing new pins at each antinode of the new eigenmode.

The half-wave fencing method is simpler to study than the antinode pinning method because it can be simulated without previous knowledge of the electric field distribution at each iteration.

3.4. Coherent leakage error probability and dispersive Purcell rate

Consider a qubit interacting with an unwanted cavity mode with coupling rate g and damping rates $\gamma_r = \gamma_d = \kappa = 0$. A quantum-mechanical representation of this system is provided by the Jaynes–Cummings Hamiltonian, the time evolution of which can be used to characterize coherent leakage errors. Assuming the cavity mode to be in the energy vacuum state $|0\rangle$ and the qubit in the energy excited state $|e\rangle$ at time $t = 0$, the time evolution of the qubit's excited state is a coherent oscillation for any value of Δ , $P_e(t, \Delta)$ with $t \geq 0$ (see appendix A.2). In this case, one possible measure of coherent leakage errors is the probability defined as

$$p = 1 - \min(P_e(t, \Delta)) \quad (3.5)$$

$$= 1 - \cos^4\left(\frac{\theta_0}{2}\right) - \sin^4\left(\frac{\theta_0}{2}\right) + 2\cos^2\left(\frac{\theta_0}{2}\right)\sin^2\left(\frac{\theta_0}{2}\right), \quad (3.6)$$

where $\theta_0 = \arctan(g/\Delta)$. The min operation on P_e ensures that (3.6) is the worst-case scenario measure of coherent leakage errors. This measure purposely neglects incoherent errors due to damped cavity modes, allowing us to determine whether the condition $p \ll \bar{p}$ for pure coherent leakage errors can be reached by means of our frequency shifting methods.

It is worth considering three limiting cases of (3.6). First, when $\Delta = 0$ or *resonant regime*, it is easy to show that $p = 1.0$, corresponding to the highest possible coherent leakage error. This occurs, for example, at the time instant when one quantum of information has completely swapped from the qubit to the cavity mode and, at that instant, the qubit was supposed to be fully excited to perform a certain algorithmic function. Second, under large detuning conditions or *dispersive regime*, $\Delta \gg g$, the error probability (3.6) can be approximated as $p \sim (g/\Delta)^2$. The purpose of the frequency shifting methods is to reach this regime in order to strongly suppress the amplitude of P_e . Third, when $\Delta \rightarrow \infty$ and for a constant g , we readily find that $p \rightarrow 0$. In this case, an ideal frequency shifting method has entirely removed any coherent leakage error due to the cavity mode.

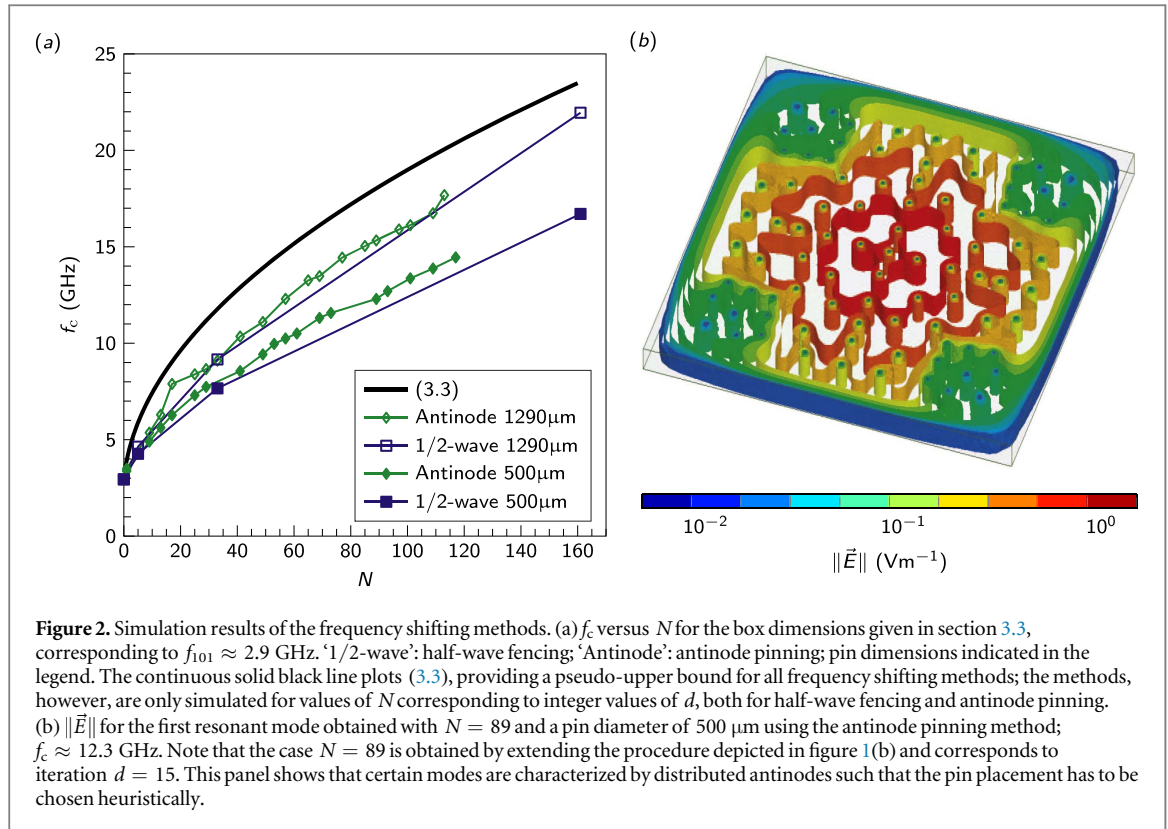
Suppose that the unwanted cavity mode is characterized by a nonzero damping rate κ . When $\Delta = 0$, depending on whether the cavity-qubit interaction is in the strong or weak coupling regime, $g \gg \kappa$ or $g \ll \kappa$, the resulting leakage errors are coherent or incoherent errors, respectively⁸. In the weak coupling regime, in particular, the presence of the mode results in the enhancement of the qubit spontaneous emission rate [34]. In the weak coupling regime with $\Delta \gg g$, instead, the cavity mode inhibits spontaneous emission, resulting in the dispersive Purcell rate [28]

$$\Gamma_c \sim \left(\frac{g}{\Delta}\right)^2 \kappa = \left(\frac{g}{\Delta}\right)^2 \frac{2\pi f_c}{Q_c}. \quad (3.7)$$

In this equation, Q_c is the quality factor of the cavity mode. We note that (3.7) remains a valid approximation as long as $\kappa \ll \Delta$, i.e., for a mode with sufficiently narrow Lorentzian linewidth (high- Q_c cavity limit). In the presence of qubit decoherence, the rate (3.7) should be engineered not to exceed the qubit bare relaxation rate, i.e., $\Gamma_c < \gamma_r$.

Assuming a fixed g , the rate (3.7) can be reduced using two approaches: increasing Δ or decreasing κ . The frequency shifting methods allow us to implement the first approach, whereas engineering the highest

⁸ The transition between the coherent and incoherent error regimes takes place for $g \sim \kappa$.



attainable Q_c makes it possible to realize the second. In the limit of $\kappa \rightarrow 0$, purely coherent leakage errors become the dominating error source. Notably, an unwanted high- Q_c cavity mode that is initially resonant with the qubit and then shifted to a large detuning condition helps protect the qubit from spontaneous emission in free space.

4. Results

In this section, we present electromagnetic field simulations of the frequency shifting methods introduced in sections 3.1 and 3.2 for a practical application (see section 4.1). We then elucidate the working principle of both methods in a realistic quantum computing configuration as well as estimate an upper bound for the corresponding coherent leakage error probability and Purcell rate (see section 4.2).

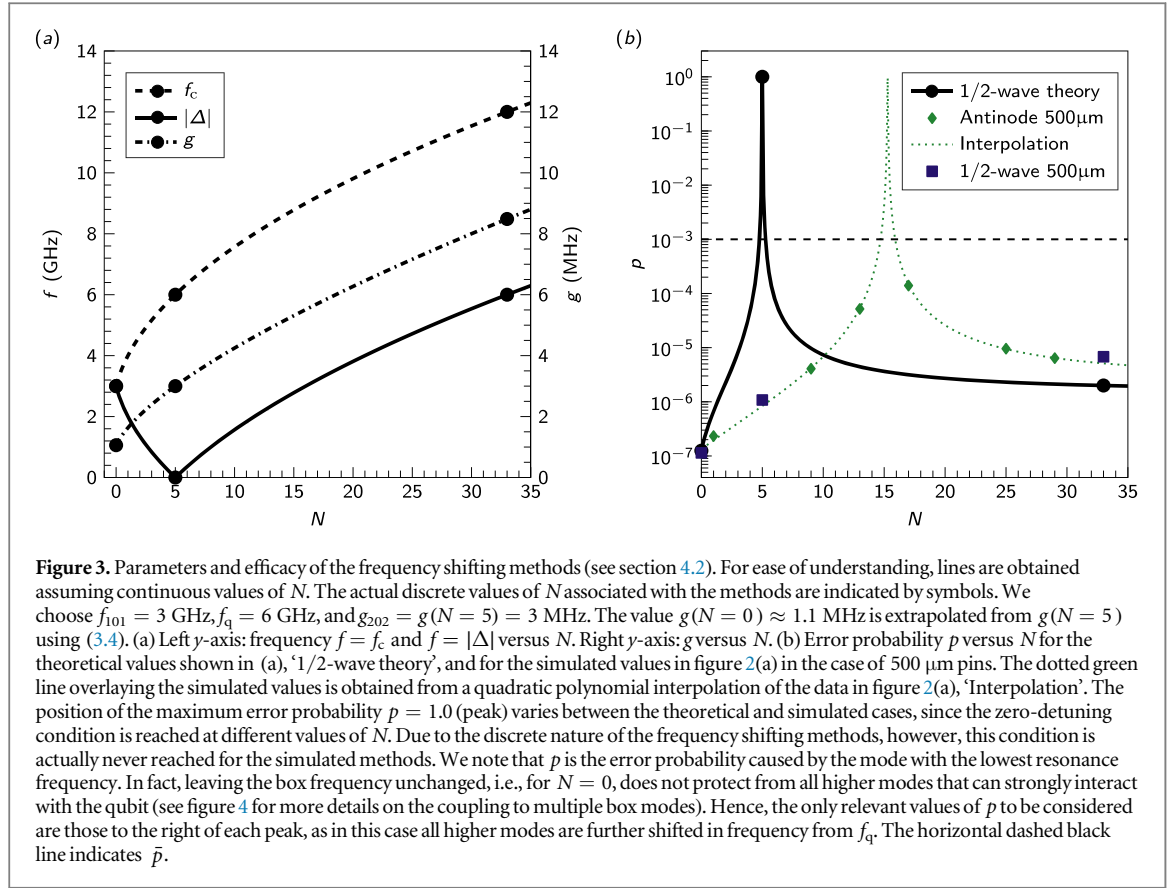
4.1. Simulations of the frequency shifting methods

The half-wave fencing method described by (3.3) is based on the assumption of fully isolated cells. In reality, however, the cylindrical shape of the coaxial Pogo pins and their finite dimensions only allow for partial fencing. In order to more accurately estimate the effectiveness of this method as well as of antinode pinning, we must resort to numerical simulations of realistic configurations. This allows us to tailor the package design to actual quantum computing applications, where it is necessary to reach a sufficiently high value of Δ such that $p \ll \bar{p}$.

Figure 2 displays simulations of the ideal box introduced in section 3.3 for pins of two different diameters. The pins with larger diameter correspond to those currently used in our packages, whereas the smaller pins are a future version planned to enable greater extensibility.

The results of the simulations show a clear correlation between pin diameter and frequency shifting, where larger pins cause a larger shift for both methods. In the case of half-wave fencing, the correlation is due to the fact that larger pins better approximate a solid wall, where each cell is more isolated from its neighbors. In addition, pins with a larger diameter modify the ideal square shape of the cell, thus perturbing the corresponding electric field that, in turn, results in a higher f_c . This effect becomes more prominent with higher values of d as the pin is proportionally bigger than each new cell size. This effect is also present in the case of antinode pinning, as bigger pins create larger new zero-potential boundary conditions. As a consequence, the relative gap between (3.3) and simulations reduces with N .

We note that the antinode pinning method provides a slight advantage over the half-wave fencing method. However, the advantage is significant only when using pins with a smaller dimension. In fact, even an



infinitesimally small pin would be sufficient to suppress an antinode, provided the perfect conductor assumption remains fulfilled.

Consider $N = 33$ pins and the box used in the simulations of figure 2. In section 3.1, we discuss the possibility to either implement half-wave fencing for $d = 2$ and, thus, realize 16 cells, or use the 33 pins to form four cells with denser picket fences. The frequency $f_c(N = 33)$ obtained with half-wave fencing for 500 μm pins can be found in figure 2(a), $f_c \approx 7.7$ GHz. Assuming the denser fences are perfect solid walls, the lowest resonance frequency for each of the four resulting cells is 6 GHz, which is significantly less than the frequency obtained from half-wave fencing. More generally, when a number of pins corresponding to an integer value of d is available, resorting to half-wave fencing is the best strategy.

Figure 2(b) displays an example of $\|\vec{E}\|$ for a box partially filled with coaxial pins, where only the outer conductor (the electrical ground) is accounted for. The electric field distribution clearly shows a situation where the optimal placement of the pins is made difficult by the complicated spatial distribution of the antinode.

In real applications, the presence of superconducting circuits and their design can impact the efficacy of the frequency shifting methods. However, these effects are very weak allowing us to use the results from idealized simulations. We support this argument by means of the nonideal-case simulations shown in appendix C.

4.2. Frequency shifting methods in a realistic quantum computing configuration

We consider a realistic quantum computing configuration, where a typical Xmon transmon qubit interacts with the modes of a box. The size of the box is purposely chosen to be sufficiently large such that $f_{101} < f_q$, thus resulting in the unwanted interaction between higher box modes and the qubit. In order to closely match the experimental scenario simulated in 4.1, we choose $f_{101} = 3$ GHz and a fixed $f_q = 2f_{101} = 6$ GHz. In this case and in absence of any additional zero-potential boundary conditions, the qubit is resonant with the fourth mode of the box (see (3.1)), $f_q = f_{202}$. An upper bound for the coupling rate between this mode and the qubit is obtained from the simulations shown in appendix B, $g_{202} = 3$ MHz. This rate is comparable or larger than other typical qubit rates, possibly leading to significant coherent leakage errors.

These errors can be mitigated using our frequency shifting methods. For simplicity, here we focus on half-wave fencing as this method can easily be represented in analytical form. Figure 3(a) displays f_c given by (3.3) and $|\Delta|$ as a function of N , where N is given by (3.2b). The discrete values of f_c increase with the corresponding values of N and, thus, of the iteration number d .

As shown in figure 1(a), iteration $d = 1$ is realized for $N = 5$, resulting in $n_c = 4$. The qubit can be positioned at any point of any of the four cells, where each cell is characterized by $f_c = f_q$. This corresponds to the *zero-detuning condition* for any of the four cell-qubit systems, $\Delta = 0$. For higher values of d , Δ increases (similarly to f_c) and a zero-detuning condition can never be reached again. This is due to the fact that we are considering the lowest resonant mode of each cell.

Assuming the qubit to be positioned at the electric field antinode of one of the four cells, we can choose the cell-qubit coupling rate to be $g(N = 5) = g_{202}$. This qubit position results in the strongest cell-qubit resonant interaction, leading to the highest coherent leakage error probabilities. As shown in figure 3(a), g increases with N due to the functional dependence of (3.4) on f_c and, thus, on N . This effect partially counteracts the benefit of the half-wave fencing method, as for larger values of N the ratio $g(N)/\Delta(N)$ decreases at a slower rate than if g were independent from N .

The coherent leakage error probability p given by (3.6) for the values of Δ and g reported in figure 3(a) is shown in figure 3(b). This panel also shows an estimate of p for the values of f_c associated with half-wave fencing and antinode pinning for 500 μm pins found from the simulations in figure 2(a). These values of f_c correspond to the lowest Δ for a given N among all scenarios simulated in section 4.1, thus resulting in an upper bound of p for the box-qubit configuration studied here. As an example, the simulated Δ obtained with half-wave fencing when $N = 33$ (i.e., $d = 2$) is sufficient to reduce p by more than two orders of magnitude compared to \bar{p} . A similar result is found for the simulated Δ due to antinode pinning when $N = 29$.

In the case of a damped box mode, our frequency shifting methods help reduce the ratio $\eta = \Gamma_c / \kappa$, where Γ_c is given by (3.7). The simulated values of g and Δ at $N = 33$ for half-wave fencing in the case of 500 μm pins, $g \approx 8.5$ MHz and $\Delta \approx 1.7$ GHz, result in $\eta \approx 2.5 \times 10^{-5}$. It has been experimentally demonstrated that superconducting boxes can reach a quality factor $Q_c > 10^8$ [35], corresponding to $\kappa \sim 1$ kHz $\ll g$. Under these conditions, coherent leakage represents the main error source due the box mode. It is not until a box damping rate $\kappa \gtrsim 10g$ that qubit decoherence due to the dispersive Purcell effect should be considered. In fact, even for a very low-quality box with $\kappa = 10g$ the resulting Purcell rate for the simulated values considered above is $\Gamma_c \approx 2.1$ kHz, which is still approximately two orders of magnitude lower than the most conservative Xmon transmon qubit energy relaxation rate $\gamma_r = 100$ kHz⁹.

5. Discussion

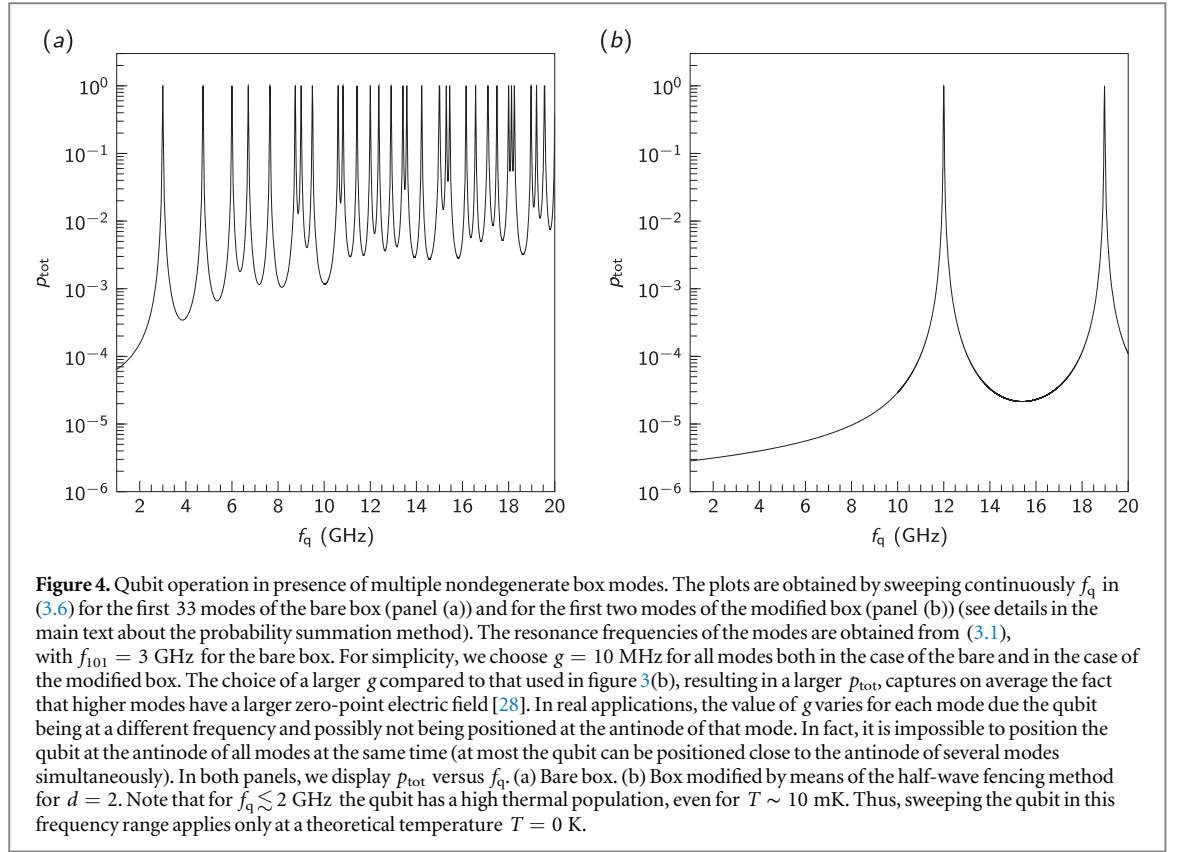
The choice of the optimal frequency shifting method depends on a variety of factors: the qubits' operation frequency; the dominant mode frequency of the package's box; the number of input and output lines required to control and measure the qubits; the size of the coaxial Pogo pins. In addition, any constraints on the qubit circuit layout can impact the pin placement.

For example, a surface code architecture comprising an array of 10×10 qubits can be realized by means of a package with approximately 250 pins and a box with dimensions $L = 72$ mm and $H = 3$ mm, as the one used in the simulations of figure 2 and introduced in [29]. This architecture is based on frequency tunable Xmon transmon qubits, assuming one XY and one Z control line per qubit and one measurement line every four qubits. In this case, the required number of pins is sufficient to shift the dominant mode frequency far enough from the typical qubit operation frequency of 6 GHz such that p is at least two orders of magnitude below \bar{p} . This result is achieved with either frequency shifting method and for any realistically sized pin. In appendix C, we demonstrate that this is the case for box sizes up to 1 m. For larger packages, and depending on the quantum processor design, it may be necessary to include ancillary pins solely devoted to frequency shifting (i.e., not used for qubit control and measurement).

Naturally, the half-wave fencing method is well suited to grid-type architectures such as, e.g., that underlying the surface code. For a 10×10 qubit array, the number of pins calculated from (3.2b) does not match the required 250 pins for any value of d . However, the half-wave fencing method can be generalized to a method where the box side L is divided by $n > 1$, the $1/n$ -wave fencing method. In this case, the quantity 2^d in (3.2a) and (3.2b) has to be substituted by n^d , and $n_c = n^{2d}$. Notably, the functional dependence of f_c on N is given by (3.3) for any value of n . Following this approach it is possible to wire up any $n \times n$ qubit array, while simultaneously mitigating coherent leakage errors.

If the available number of pins is the limiting resource, antinode pinning is the ideal method of choice. In fact, it typically results in the greatest return on pin count, particularly when using small pins. Additionally, this is the most appropriate method when the constraints on the circuit layout are very restrictive. Suppose, for example, the user must initially place a set of pins at specific locations, ignoring any frequency shifting method.

⁹ This corresponds to a qubit relaxation time $T_1 = 10$ μs .



This scenario can be treated as the $d = 0$ iteration of the antinode pinning method, thus making the method suitable for cavities of arbitrary shape.

It is also worth noting that the two frequency shifting methods are not mutually exclusive. Instead, they can be combined depending on the user requirements. If the $1/n$ -wave fencing method only partially meets the wire requirements of an arbitrary two-dimensional array of qubits, the wiring can be completed by means of antinode pinning. This, for example, is a good strategy when N does not correspond to any integer value of d in (3.2b). In this case, the available pins can be used to form as many fully $1/n$ -wave fenced cells as possible, with the residual pins implementing antinode pinning.

We note that the effect of the frequency shifting methods on higher cavity modes must also be taken into account. In fact, the frequency shift relative to higher modes is lowered relative to the shift for the dominant mode. This can result in a qubit being dispersively coupled to, e.g., m modes, with higher modes closer to each other in frequency. In absence of any damping, we can assume these modes to act as multiple independent leakage channels. In this case, assuming the coherent leakage error probability for all m modes being considered to be equal to the error probability p of the dominant mode (this is a worst-case scenario assumption since p is smaller for higher modes), the total error probability can be estimated to be $\sim mp$. According to the results in figure 3(b), we can easily tolerate up to $m \sim 100$.

In order to clearly show the effect of higher cavity modes on the operation of one qubit, we consider a box with $f_{101} = 3$ GHz and sweep f_q over a wide range from 1 to 20 GHz, which comprises 60 box modes for a bare box (i.e., where no frequency shifting method is applied). Among these 60 modes, 27 are degenerate and, thus, discarded. In fact, in our definition of g we assume the qubit to be positioned at a mode antinode. It is therefore physically impossible to simultaneously couple the same qubit to any pair of degenerate modes¹⁰. Figure 4 is generated using (3.6) for each of the resulting 33 nondegenerate modes. In the dispersive regime regions, the total error probability p_{tot} is obtained by summing the error probability of all modes assuming the probabilities to be independent from each other; in the semi-resonant regime regions, p_{tot} is that of the only mode on or close to resonance with the qubit. The plot in figure 4(a) further clarifies that the low error probability for $f_c \ll f_q$ in the case of a bare box, as shown in figure 3(b), is only possible when considering the coupling to the lowest resonant mode. However, the presence of higher modes for the same box size is highly detrimental to the qubit operation. The plot in figure 4(b) demonstrates that half-wave fencing for $d = 2$ makes it possible to operate the qubit safely at all frequencies $\lesssim 10$ GHz, since, in this case, the resonance frequency of the lowest and of all higher box modes is well above this frequency.

¹⁰ Mode nml is degenerate with mode lmn . Degenerate modes have the same resonance frequency and orthogonal nodal lines.

In presence of damped cavity modes, the scenario differs depending on the magnitude of the damping rate of each mode. In case of low damping, i.e., κ is much smaller than the frequency separation between two consecutive modes and up to a cutoff mode \bar{m} (for higher modes the detuning is large enough that the dispersive Purcell rate associated with them can be neglected), the total dispersive Purcell rate for these modes is given by $\sim \sum_{j=1}^{\bar{m}} \Gamma_{cj}$, where Γ_{cj} is the Purcell rate of the j th mode [36]. For example, assuming a mean dispersive Purcell rate $\langle \Gamma_c \rangle \sim 1$ kHz for all modes up to \bar{m} (see estimate in section 4.2), we can tolerate up to $\bar{m} \sim 100$ before the Purcell rate starts impacting qubit decoherence. When κ becomes large enough that the modes strongly overlap with each other, this set of modes should be treated as a continuous mode distribution.

An unwanted cavity mode can also mediate interactions between pairs of (or even multiple) qubits. As explained in appendix A.1, the corresponding dynamics can lead to correlated errors. The frequency shifting methods introduced here allow the separation of the qubits transition frequency from the cavity resonance frequency such that the qubit-cavity-qubit interaction gives rise only to virtual transitions. This result is similar to the dispersive two-qubit \sqrt{i} SWAP gate introduced in [28]. Assuming both qubits are coupled with the same coupling coefficient g to the cavity mode, the worst-case scenario is when the qubits are in resonance with each other and detuned by Δ from the mode. The effective qubit-qubit coupling strength is then g^2/Δ (dispersive coupling), which is strongly suppressed for values of Δ larger than several times g .

Our frequency shifting methods are directly applicable to the problem of dielectric substrate modes, which has been addressed qualitatively in [37]. In this case, the resonance frequency of the substrate modes is given by (3.1) replacing c with $c/\sqrt{\epsilon_r}$, where ϵ_r is the relative permittivity of the substrate. The pins must be replaced by superconducting vias [17, 32], with all other methodological requirements remaining unchanged. The number of vias embedded in the substrate will need to be significantly higher than the number of pins in free space due to the lower frequency of the dominant mode. Notably, fabricating a large array of vias is a relatively simple process that can be made compatible with standard qubit fabrication techniques.

Finally, it is worth commenting on the possibility to reduce leakage errors due to unwanted cavity modes by decreasing the cavity-qubit coupling rate g . There are three main approaches to reduce g : first, place the qubits only in proximity of cavity field nodes; second, increase H thereby decreasing (3.4); third, modify the qubit geometry to decrease $\beta = C_g/(C_g + C_p)$ for a constant value of H , where C_g and C_p are the capacitances between the transmon capacitive island and the box top and bottom walls, respectively (see also appendix B). The first approach is impractical as it severely limits the available space on the chip. In order to be useful, the second approach can easily lead to new unwanted cavity modes. In the case of transmon qubits, the third approach strongly affects the qubit charging energy possibly having detrimental effects on its decoherence properties and anharmonicity.

6. Conclusion

In this work, we study theoretically and with simulations a category of errors, leakage errors, which becomes increasingly important with larger quantum computing architectures. We consider large packages where coaxial Pogo pins allow the operation of 100 or more superconducting qubits. We propose two methods, half-wave fencing and antinode pinning, that make it possible to reduce the effect of unwanted box modes by means of the same pins used for qubit control and measurement. For example, the 250 pins required to operate a 100 qubit processor reduce coherent leakage error to probabilities below $\sim 10^{-5}$, which are significantly lower than the state-of-the-art error probabilities for superconducting qubit operations. Similarly, our methods allow us to reduce the effect of damped modes up to two orders of magnitude below the typical decoherence rates of superconducting qubits.

Our simulations demonstrate that unwanted modes for boxes as big as $1\text{ m} \times 1\text{ m}$ can be mitigated using the frequency shifting methods. It is worth noting that our methods can be combined with the modular architecture proposed in [16], where boxes containing hundreds of qubits are coupled together to form systems with thousands of qubits. The frequency shifting methods can also be used to mitigate the effects of substrate modes, another important source of errors in extensible superconducting qubit architectures.

In future projects, it will be necessary to gain further insight into the effects due to multiple discrete and continuous mode distributions. Additionally, it will be necessary to study the detrimental effects of unwanted box and substrate modes by measuring leakage errors affecting superconducting qubits. A sensitive method to perform such measurements is reported in [38]. Extending this method to larger substrates and bigger boxes will allow us to verify the effectiveness of the frequency shifting methods in a realistic quantum computing scenario.

Acknowledgments

This research was undertaken thanks in part to funding from the Canada First Research Excellence Fund (CFREF) and the Discovery Grant Program of the Natural Sciences and Engineering Research Council of Canada (NSERC). We would like to acknowledge the Canadian Microelectronics Corporation (CMC) Microsystems for the provision of products and services that facilitated this research, including CAD software and HFSS. MM acknowledges his fruitful discussions with Joseph Emerson and Austin G Fowler. We thank Evan A Peters for his comments on the manuscript.

Appendix A. Qubit coherent errors and the Jaynes–Cummings model

In this appendix, we summarize the main concepts of qubit coherent errors (see appendix A.1) and recapitulate the Jaynes–Cummings model (see appendix A.2).

A.1. Qubit coherent errors

In a quantum computer, the Hilbert space of all qubits and any other internal auxiliary system required to operate them is defined as the *computational subspace*; on the contrary, the space associated with any external system interacting with the qubits is called the *leakage subspace* [24]. In general, the time evolution of a qubit interacting with internal and external systems is described by the combination of a purely unitary generator \mathcal{H} and a purely dissipative generator \mathcal{D} [24, 27].

The generator \mathcal{H} accounts for the qubit Hamiltonian as well as the Hamiltonian of any wanted or unwanted internal system or any external system, or both. External systems always lead to unwanted dynamics and, thus, to qubit errors, whereas only unwanted internal systems generate qubit errors. The purely unitary nature of \mathcal{H} results in coherent dynamics, implying that all the errors associated with it are *coherent errors*. In particular, errors due to external systems are called *coherent leakage errors*. The generator \mathcal{D} , instead, describes external environments acting as stochastic phenomena (e.g., Markovian noise). Therefore, the qubit errors associated with \mathcal{D} are defined as *incoherent leakage errors*; these errors are typically due to qubit decoherence, i.e., relaxation and dephasing [4, 5]. Note that two- or multi-qubit *correlated errors* can also exist [21]. In this case, when an error occurs on one qubit it affects one or more different qubits in the quantum computer. Correlated errors can stem from either coherent or incoherent dynamics.

In superconducting qubit implementations, a typical example of a wanted internal system is a resonator acting as a quantum bus between pairs of qubits [39]. The states of the bus are populated during computations, although at the end of any computation only qubits' states remain populated. A special class of wanted internal systems is represented by classical driving electromagnetic fields used to control and measure the qubit's state. These systems result in unwanted dynamics when leading to stray fields that act on undesired qubits [40]. An example of an external system, instead, is a cavity mode due to the box used to house a superconducting qubit device. This mode can also generate correlated errors between a pair of qubits that interact with it independently.

A.2. The Jaynes–Cummings model

The system comprising an unwanted cavity mode coupled to a qubit can be represented by the Jaynes–Cummings model. We assume the cavity-qubit interaction Hamiltonian to be an electric-dipole Hamiltonian \hat{H}_{ed} with coupling rate $g = E_0 p_q / \hbar$, where [41]

$$E_0 = \left(\frac{\hbar f_c}{2\epsilon_0 V} \right)^{1/2} \quad (\text{A.1})$$

is the zero-point electric field of a cavity with volume V and a qubit with effective electric-dipole moment p_q [28]. In our definition of g , the qubit is assumed to be at an antinode of the cavity electric field.

In the interaction picture with respect to the cavity and qubit Hamiltonians (and with our definition of Δ), the Jaynes–Cummings Hamiltonian reads

$$\hat{H}_{\text{JC}} = \hbar \frac{g}{2} (\hat{a}^\dagger \hat{\sigma}^- e^{+i2\pi\Delta t} + \hat{a} \hat{\sigma}^+ e^{-i2\pi\Delta t}), \quad (\text{A.2})$$

where \hat{a}^\dagger and \hat{a} are the electromagnetic field creation and annihilation operators of the cavity mode, whereas $\hat{\sigma}^-$ and $\hat{\sigma}^+$ are the lowering and raising operators acting on the energy ground state $|g\rangle$ and excited state $|e\rangle$ of the qubit.

When the cavity-qubit system is prepared in the one excitation sector, the first two energy eigenstates or *dressed states* of the system are obtained from the exact diagonalization of \hat{H}_{JC} ,

$$|0, -\rangle = \cos\left(\frac{\theta_0}{2}\right)|1, g\rangle - \sin\left(\frac{\theta_0}{2}\right)|0, e\rangle, \quad (\text{A.3})$$

$$|0, +\rangle = \sin\left(\frac{\theta_0}{2}\right)|1, g\rangle + \cos\left(\frac{\theta_0}{2}\right)|0, e\rangle. \quad (\text{A.4})$$

The states $|1, g\rangle$ and $|0, e\rangle$ are called *bright states* of the Jaynes–Cummings model, whereas state $|0, g\rangle$ is a *dark state*.

The energy eigenvalues associated with (A.3) and (A.4) are given by

$$E_{0,\mp} = hf_c \mp h\alpha_0, \quad (\text{A.5})$$

where $\alpha_0 = \sqrt{g^2 + \Delta^2}/2$. The energy eigenvalue for $|0, g\rangle$ is $E_{0,g} = h\Delta/2$.

In the Schrödinger picture, the time evolution of a general cavity-qubit state can be written as

$$|\psi(t)\rangle = e^{-i\pi f_c t} \left[\cos\left(\frac{\theta_0}{2}\right)|0, +\rangle e^{-i\alpha_0 t} - \sin\left(\frac{\theta_0}{2}\right)|0, -\rangle e^{+i\alpha_0 t} \right]. \quad (\text{A.6})$$

Assuming an ideal qubit measurement, the time evolution of $|0, e\rangle$, $P_{0,e}(t)$, is equivalent to $P_e(t, \Delta)$,

$$\begin{aligned} P_{0,e}(t) &= |\langle 0, e | \psi(t) \rangle|^2 = P_e(t, \Delta) = \cos^4\left(\frac{\theta_0}{2}\right) + \sin^4\left(\frac{\theta_0}{2}\right) \\ &\quad + 2\cos^2\left(\frac{\theta_0}{2}\right)\sin^2\left(\frac{\theta_0}{2}\right)\cos(4\pi\alpha_0 t). \end{aligned} \quad (\text{A.7})$$

This is the equation we use to find (3.6).

Appendix B. Estimate of box-qubit coupling rates

In this appendix, we estimate a typical box-qubit coupling rate by emulating an Xmon transmon qubit by means of the microwave structure depicted in figure B1(a) and simulating its interaction with a box mode. The structure comprises a coplanar waveguide (CPW) cross on the xz -plane, with the center bottom attached to a micro-coaxial half-wave resonator of length R that extends outside the box, along the y -axis. The cross acts as an ‘antenna’ that couples to the box modes with resonance frequencies given by (3.1), which are set by the geometry of the box. By continuously varying R , it is possible to sweep the resonance frequency of the resonator, f_R , resulting in a tunable resonator coupled to a set of fixed box modes. The cross lies on the same plane as the metallic bottom wall of the box, with a dielectric substrate directly below. The center of the cross is positioned at the antinode of the electric field of the dominant mode. The dimensions of the CPW cross are the center conductor width S , the gap width W , and the arm length A ; the substrate is characterized by a thickness t_s and relative permittivity ϵ_r .

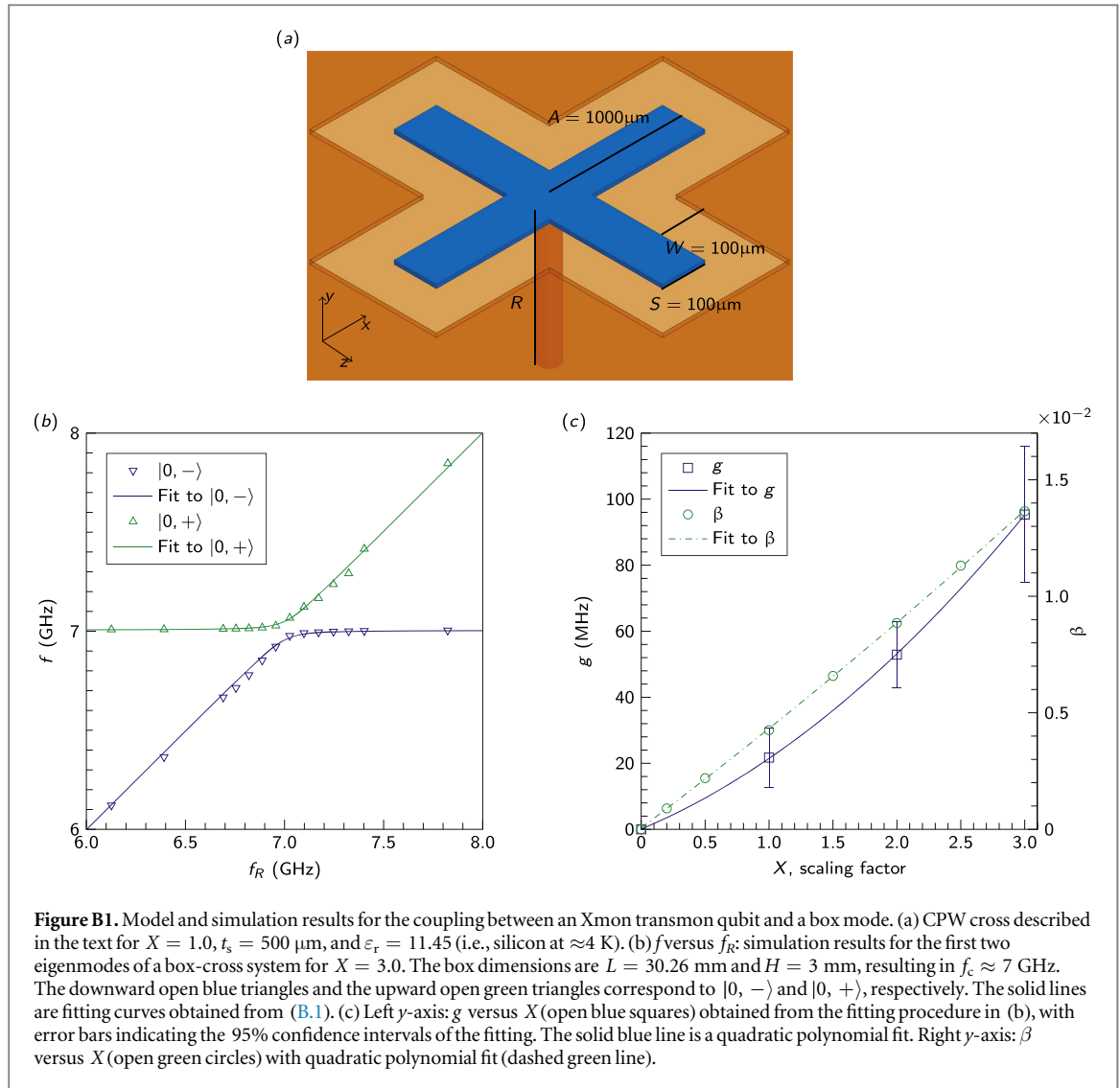
We perform electromagnetic field simulations of the cross-box coupled system by means of HFSS. We sweep f_R through f_c obtaining the first two eigenmodes. An accurate simulation of this system is computationally intensive due to the high aspect ratio between the largest and smallest features of the system ($\sim 10 \text{ mm}/10 \text{ }\mu\text{m}$). This issue can be overcome by scaling up the dimensions of the cross, while maintaining the same box size. The dimensions of each simulated cross are determined from $S/X = W/X = 100 \text{ }\mu\text{m}$ and $A/X = 1000 \text{ }\mu\text{m}$, where X is a scaling factor (see figure B1(a) for numerical values). We simulate the coupled system for progressively smaller cross dimensions until exceeding the capabilities of our computer. Values of g for even smaller cross sizes can be extrapolated following the trend established by the simulated systems.

The first two eigenmodes of the electric field for $X = 3.0$ are shown in figure B1(b). This diagram resembles the energy level anti-crossing of a coupled cavity-qubit system. Thus, it can be used to estimate g by fitting the simulated frequency eigenmodes to the frequencies associated with the first two energy dressed states of the Jaynes–Cummings Hamiltonian \hat{H}_{JC} , $|0, -\rangle$ and $|0, +\rangle$, respectively, subtracted by the frequency of the ground state energy (see appendix A.2),

$$\bar{f}_{0,\mp} = \frac{E_{0,\mp} - E_{0,g}}{h} = \left(f_c \mp \alpha_0 - \frac{\Delta}{2} \right). \quad (\text{B.1})$$

The curve fitting results are shown in figure B1(b), where the Jaynes–Cummings model overlays the simulated data.

We perform the simulation and curve fitting procedure for three different values of X . The corresponding values of g are displayed in figure B1(c) that also shows a quadratic polynomial fit of the data, allowing the estimation of g for other values of X . The electric field sinusoidal distribution is taken into account in the simulations.



For the parameter space chosen in the simulations, our scaling argument and derived coupling values are consistent with those in [42]. In that study, it is shown that a change in transmon qubit geometry is equivalent to a change in the capacitance ratio $\beta = C_g/(C_g + C_p)$ for a constant box height H . This ratio accounts for the capacitances C_g and C_p between the CPW cross (i.e., the transmon qubit capacitive island) and the box top and bottom walls, respectively, and directly relates to a change in g . We calculate β from C_g and C_p obtained for the values of X used to find g , as well as for additional intermediate values. The capacitances C_g and C_p are simulated with ANSYS Q3D Extractor¹¹. The results are shown in figure B1(c). The figure also displays a quadratic polynomial fit of the simulated data, allowing us to compare the relationship between β and g . In spite of a slight mismatch, the results are sufficiently accurate to provide an upper bound for the coupling coefficient of a typical Xmon transmon qubit.

Appendix C. Nonideal-case simulations and scalable implementation

In the main text, we focus on realistic yet idealized scenarios that allow us to easily understand the working principles and the general efficacy of the proposed frequency shifting methods. In order to unveil any possible limitations, in this appendix we study nonideal cases where the methods are tested in more realistic and even extreme conditions.

Three main cases are considered: first, we simulate very large boxes to ensure the methods are compatible with scaled architectures; second, we analyze a package that houses a substrate patterned with overly large circuits to show that the perturbation to the box modes from exposed dielectric does not significantly reduce the effectiveness of the methods; third, we provide the actual circuit design of an array of Xmon transmon qubits

¹¹ See <http://ansys.com/Products/Electronics/ANSYS-Q3D-Extractor> for details on Q3D.

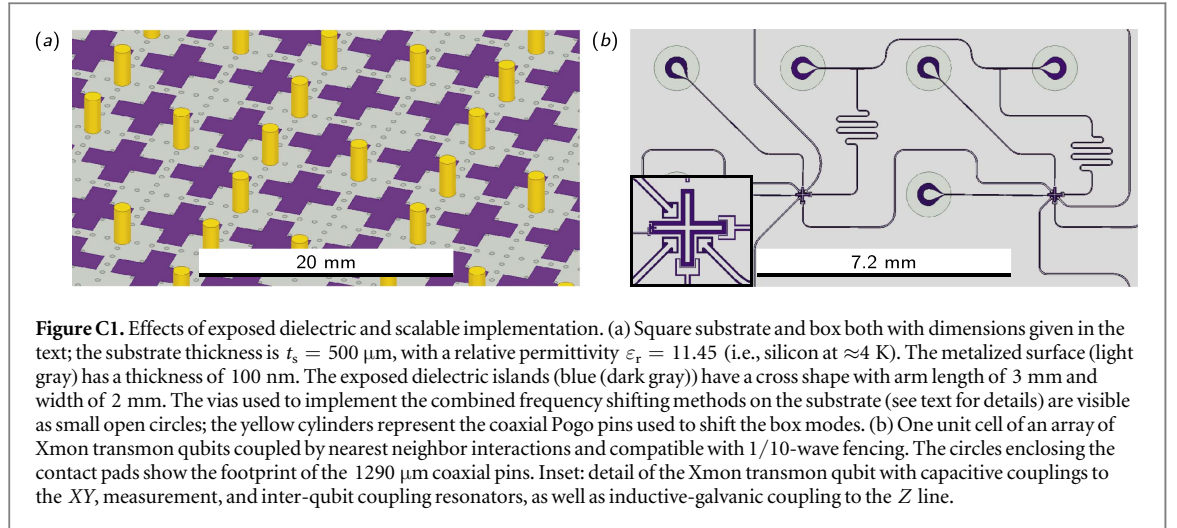


Table C1. Approximate value of f_c for two large boxes with different lateral dimensions L applying the half-wave fencing method for different iterations d .

d	f_c for $L = 0.25 \text{ m}$ (GHz)	f_c for $L = 1 \text{ m}$ (GHz)
0	0.9	0.2
1	1.2	0.3
2	2.1	0.5
3	4.5	0.9
4	10.6	2.0
5	26.8	4.5

with all necessary circuitry for a surface code architecture and propose a frequency shifting method tailored to this implementation.

In all simulations presented in this appendix, we resort to less stringent convergence requirements in order to reach successful completion on our computers. While this choice results in greater margins of error, it still allows us to draw convincing conclusions on the potential limitations of the methods.

To verify that our frequency shifting methods can be used for almost arbitrarily large cavities, we simulate half-wave fencing assuming two different boxes with dimensions $L = 0.25 \text{ m}$ and $L = 1 \text{ m}$, in both cases with $H = 3 \text{ mm}$. The results are reported in table C1. For iteration $d = 5$, we find $f_c \approx 26.8 \text{ GHz}$ and $\approx 4.5 \text{ GHz}$ for the small and large box, respectively. We are not able to simulate larger values of d for the large box due to the computational cost of the simulation. Even though, in this case, $d = 5$ is insufficient to increase f_c above the typical qubit frequencies, the simulation trend shown in table C1 is very comforting. In fact, by fitting the values in the table using (3.3) with a multiplicative reduction factor as a single fitting parameter (that accounts for the differences between theory and realistic simulations), we find that $d = 6$ results in at least $f_c \approx 8.7 \text{ GHz}$. More generally, we conjecture that our frequency shifting methods are effective regardless of the lateral dimensions of the cavity.

Consider, for example, the $1 \text{ m} \times 1 \text{ m}$ box and the surface code architecture in [29], which is characterized by a distance between adjacent pairs of pins of 1 mm with a density of four Xmon transmon qubits per $8 \text{ mm} \times 8 \text{ mm}$ cell. In this case, the number of pins required to address the 126×126 qubit array is $39\,690$, whereas the number of pins required for half-wave fencing with $d = 6$ is only $N = 12\,033$.

When considering a package that houses a substrate enclosed in a similarly sized box, treating box and substrate modes separately is a suitable assumption only if the substrate surface is completely metalized. In real applications, typical circuit designs naturally result in regions of exposed dielectric that perturb the box modes. However, the ratio between the area of exposed dielectric and metalized ground plane is small enough not to significantly perturb the mode resonance frequencies. We confirm this argument by simulating a substrate patterned with abnormally large sections of exposed dielectric, as shown in figure C1(a). The results are compared to the idealized case, with and without the implementation of the frequency shifting methods.

Table C2. Approximate value of f_c for an ‘isolated box’ and for a box perturbed by exposed dielectric or ‘perturbed system’. In both cases, we apply the 1/5-wave fencing method for different iterations d .

d	f_c for isolated box (GHz)	f_c for perturbed system (GHz)
0	2.94	2.82
1	11.97	11.81

When no methods are applied, the modes with lowest resonance frequency are those associated with the substrate due to its relative permittivity. In this case, we determine the box mode with lowest resonance frequency by plotting $\|\vec{E}\|$ for a few possible modes and selecting the one with closest resemblance to a TE_{101} box mode.

The following methods are then applied: 1/5-wave fencing for the box; 1/10-wave fencing for the substrate in combination with antinode pinning for $d = 2$ within each 1/10-wave fenced cell. Note that, in this case, we cannot apply antinode pinning for $d = 1$ because the simulated circuit is located at the field antinode. Although this combination of methods is suboptimal in terms of frequency shifting, it is the easiest for the abnormal circuits considered in these simulations. By means of the combined frequency shifting methods, we ensure that the lowest substrate mode frequency is higher than the lowest box mode frequency. The simulation results are reported in table C2. The impact of the exposed dielectric on f_c is ≈ 120 MHz and ≈ 160 MHz with or without frequency shifting methods, respectively.

In order to understand whether the presence of superconducting circuitry can impact the frequency shifting methods significantly, we consider the quantum-mechanical interaction between the qubits and cavity modes in the dispersive regime. Assume an array of 1000 qubits all strongly, but (for simplicity) independently interacting with an unwanted cavity mode with coupling rate $g \sim 10$ MHz. Suppose a frequency shifting method results in $\Delta \sim 1$ GHz, the AC Stark shift of the mode resonance frequency due to each qubit is $\Delta f \sim (g^2/\Delta)\hat{\sigma}_z$, where $\hat{\sigma}_z$ is the usual Pauli matrix. Depending on the qubit state, $\hat{\sigma}_z$ simply changes the sign of the Stark shift. Under these conditions, the total frequency shift can be estimated by multiplying the shift due to one qubit by 1000, resulting in a maximum shift $\Delta f \sim \mp 100$ MHz (all qubits are either in the ground or excited state). This shift is similar to those generated by exposed dielectric reported in table C2. Thus, we conclude that treating the box and substrate modes independently and, to a good extent, ignoring the design details of specific circuit layouts is a reasonable idealization.

We then consider a 10×10 array of Xmon transmon qubits realized on a $72 \text{ mm} \times 72 \text{ mm}$ substrate that is enclosed in a box with the same lateral dimensions. A frequency shifting method compatible with this configuration is 1/10-wave fencing for $d = 1$. This method leads to fences of pins running along the gaps between neighboring qubits. A simulation of this configuration gives $f_c \approx 29.7$ GHz. Figure C1(b) shows one unit cell of the array for one XY and one Z control line per qubit, one measurement line every two qubits, and one coupling resonator between each pair of qubits (see [29] for a similar design). The unit cell can be repeated to form much larger arrays while maintaining $f_c \gg f_q$. Note that most of the metalization of the substrate surface is used as a ground plane, with very little exposed dielectric. Dielectric exposure is further decreased since the contact pads are covered by the coaxial Pogo pins. Additionally, there is ample space for via placement making it possible to apply a suitable frequency shifting method to mitigate the effect of substrate modes.

Finally, we consider a qubit array based on transmon qubits fixed in frequency, requiring only one Pogo pin per qubit and a generous spacing of 2 mm between adjacent qubits (see, e.g., the architecture of [20]). In this architecture, an applicable frequency shifting method for an $n \times n$ array of qubits is a $3/n$ -wave fencing for $d = 1$ followed by antinode pinning for $d = 1$. This results in a repeating cell that encapsulates nine qubits, where each qubit is addressed by one single pin. The f_c from only applying $3/n$ -wave fencing is already far above any typical f_q as the resulting cell size is $4 \text{ mm} \times 4 \text{ mm}$. This example shows that our frequency shifting methods are also possibly compatible with future architectures that make advances in control and measurement electronics and, thus, require fewer wires per qubit.

ORCID iDs

M Mariani  <https://orcid.org/0000-0002-9235-5719>

References

- [1] Nielsen M A and Chuang I L 2000 *Quantum Computation and Quantum Information* (Cambridge: Cambridge University Press)
- [2] Montanaro A 2016 *NPJ Quantum Inf.* **2** 15023
- [3] Ladd T D, Jelezko F, Laflamme R, Nakamura Y, Monroe C and O’Brien J L 2010 *Nature* **464** 45–53

- [4] Clarke J and Wilhelm F K 2008 *Nature* **453** 1031–42
- [5] Wendin G 2017 *Rep. Prog. Phys.* **80** 106001
- [6] Kelly J et al 2015 *Nature* **519** 66–9
- [7] Gambetta J M, Chow J M and Steffen M 2017 *NPJ Quantum Inf.* **2**
- [8] Barends R et al 2013 *Phys. Rev. Lett.* **111** 080502
- [9] Kamal A, Yoder J L, Yan F, Gudmundsen T J, Hover D, Sears A P, Welander P, Orlando T P, Gustavsson S and Oliver W D 2016 Improved superconducting qubit coherence with high-temperature substrate annealing arXiv:1606.09262
- [10] Gambetta J M, Murray C E, Fung Y K K, McClure D T, Dial O, Shanks W, Sleight J W and Steffen M 2017 *IEEE Trans. Appl. Supercond.* **27** 1–5
- [11] Barends R et al 2014 *Nature* **508** 500–3
- [12] Jeffrey E et al 2014 *Phys. Rev. Lett.* **112** 190504
- [13] Fowler A G, Mariantoni M, Martinis J M and Cleland A N 2012 *Phys. Rev. A* **86** 032324
- [14] Gottesman D 2010 *Quantum Information Science and Its Contributions to Mathematics, Proc. Symp. in Applied Mathematics* vol 68, pp 13–58
- [15] Boixo S, Isakov S V, Smelyanskiy V N, Babbush R, Ding N, Jiang Z, Bremner M J, Martinis J M and Neven H 2017 Characterizing quantum supremacy in near-term devices arXiv:1608.00263
- [16] Brecht T, Pfaff W, Wang C, Chu Y, Frunzio L, Devoret M H and Schoelkopf R J 2016 *NPJ Quantum Inf.* **2** 16002
- [17] Versluis R, Poletto S, Khammassi N, Tarasinski B, Haider N, Michalak D J, Bruno A, Bertels K and DiCarlo L 2017 *Phys. Rev. Appl.* **8** 034021
- [18] Rosenberg D et al 2017 *NPJ Quantum Inf.* **42**
- [19] McDermott R, Vavilov M G, Plourde B L T, Wilhelm F K, Liebermann P J, Mukhanov O A and Ohki T A 2018 *Quantum Sci. Technol.* **3** 024004
- [20] Bronn N T, Adiga V P, Olivadese S B, Wu X, Chow J M and Pappas D P 2018 *Quantum Sci. Technol.* **3** 024007
- [21] Fowler A G and Martinis J M 2014 *Phys. Rev. A* **89** 032316
- [22] Orsucci D, Tiersch M and Briegel H J 2016 *Phys. Rev. A* **93** 042303
- [23] Greenbaum D and Dutton Z 2018 *Quantum Sci. Technol.* **3** 015007
- [24] Wood C J and Gambetta J M 2018 *Phys. Rev. A* **97** 032306
- [25] Wenner J et al 2011 *Supercond. Sci. Technol.* **24** 065001
- [26] Abraham D W, Chow J M, Gonzalez A D C and Gambetta J M 2015 Frequency separation between qubit and chip mode to reduce Purcell loss US9159033B2
- [27] Rivas Á and Huelga S F 2012 *Open Quantum Systems* (Berlin: Springer) (<https://doi.org/10.1007%2F978-3-642-23354-8>)
- [28] Blais A, Huang R S, Wallraff A, Girvin S M and Schoelkopf R J 2004 *Phys. Rev. A* **69** 062320
- [29] Béjanin J H et al 2016 *Phys. Rev. Appl.* **6** 044010
- [30] Foxen B et al 2018 *Quantum Sci. Technol.* **3** 014005
- [31] O'Brien W 2017 Superconducting caps for quantum integrated circuits arXiv:1708.02219
- [32] Vahidpour M 2017 Superconducting through-silicon vias for quantum integrated circuits arXiv:1708.02226
- [33] Collin R E 2001 *Foundations for Microwave Engineering* 2nd (Hoboken, NJ, New York: Institute of Electrical & Electronics Engineers (IEEE), Wiley) (<https://doi.org/10.1109/9780470544662>)
- [34] Goldstein E V and Meystre P 1995 Spontaneous emission in optical cavities: a tutorial review *Spontaneous Emission and Laser Oscillation in Microcavities (Laser & Optical Science & Technology)* ed H Yokoyama and K Ujihara (Boca Raton, FL: CRC Press) pp 1–46
- [35] Reagor M 2013 *Appl. Phys. Lett.* **102** 192604
- [36] Sundaresan N M, Liu Y, Sadri D, Szöcs L J, Underwood D L, Malekakhlagh M, Türeci H E and Houck A A 2015 *Phys. Rev. X* **5** 021035
- [37] Abraham D W, Keefe G A, Lavoie C and Rothwell M E 2014 Chip mode isolation and cross-talk reduction through buried metal layers and through-vias US20140274725A1
- [38] Sheldon S, Sandberg M, Paik H, Abdo B, Chow J M, Steffen M and Gambetta J M 2017 *Appl. Phys. Lett.* **111** 222601
- [39] Mariantoni M et al 2011 *Science* **334** 61–5
- [40] Najafi-Yazdi A, Kelly J and Martinis J 2017 High fidelity, numerical investigation of cross talk in a multi-qubit Xmon processor meetings.aps.org/Meeting/MAR17/Session/C46.9
- [41] Haroche S and Raimond J M 2006 *Exploring the Quantum* (Oxford: Oxford University Press) (<https://doi.org/10.1093/acprof:oso/9780198509141.001.0001>)
- [42] Brecht T, Chu Y, Axline C, Pfaff W, Blumoff J Z, Chou K, Krayzman L, Frunzio L and Schoelkopf R J 2017 *Phys. Rev. Appl.* **7** 044018